PERGAMON

International Journal of Heat and Mass Transfer 42 (1999) 833–853

International Journal of HEAT and MASS TRANSFER

Lid-driven cavity with heat and mass transport

N. Alleborn*, H. Raszillier, F. Durst

Lehrstuhl für Strömungsmechanik, Universität Erlangen-Nürnberg, Cauerstrasse 4, 91058 Erlangen, Germany

Received 7 January 1998; in final form 7 July 1998

Abstract

The configurations of steady two-dimensional flow accompanied by heat and mass transport in a shallow lid-driven cavity with a moving heated lid and a moving cooled lid were investigated numerically in a process engineering context of drying. A continuation method was applied to track the branches of the diagram of flow configurations in their dependence on various parameters and to determine their linear stability by an Arnoldi-based method. Analytical solutions for limiting situations of the geometrical and flow parameters, obtained by computer algebra, were compared with numerical results. In a parameter study for horizontal and vertical orientation of the cavity, the dependence of heat and mass transfer rates on the velocities of the walls and on the species concentration boundary conditions was investigated. Among the results found, for a vertical cavity, there are two turning points and flow configurations with minimal heat and mass transfer, and for a horizontal cavity heated from below a Hopf bifurcation indicating inception of oscillatory flow regimes.

Nomenclature

a_i coefficients in series expansion
C normalized concentration defined by equation (9)
D diffusion coefficient
$\mathbf{e}_x$, $\mathbf{e}_y$ unit vectors
g gravitational acceleration
g gravity vector
Gr Grashof number defined by equation (6)
h heat transfer coefficient
H cavity height
k_ω mass transfer coefficient
L cavity length
l cavity aspect ratio, $l = L/H$
$\dot{m}_j$ mass flux per unit width ($j = c, e$)
M_j dimensionless mass flux per unit width ($j = c, e$)
Nu Nusselt number defined by equation (28)
Pr Prandtl number defined by equation (2)
Pe Peclet number, $Pe = RePr$
$\dot{q}_j$ heat flux ($j = c, e$)
Q_j dimensionless heat flux ($j = c, e$)
Re Reynolds number defined by equation (4)
Sc Schmidt number defined by equation (3)
Sh Sherwood number defined by equation (29)
t time
T_j (absolute) temperatures of the walls ($j = c, e$) [K]
U_j velocities of the walls ($j = c, e$)
u velocity ratio, $u = U_c/U_e$
u_x, u_y dimensionless velocity components
v constant dimensionless velocity defined by equation (42)
x, y dimensionless coordinates
x_d entrance length
x_v virtual origin.

Greek symbols

α angle, defining the orientation of the cavity
β_v coefficient of thermal expansion
Γ concentration parameter defined by equation (7)
κ thermal diffusivity
λ thermal conductivity
λ_i eigenvalue
ν kinematic viscosity
$\phi_i(y)$ eigenfunction
ψ streamfunction
ρ density of the gas mixture
σ growth rate
ν normalized temperature defined by equation (9)
ω solvent vapor mass fraction
ω_j solvent vapor mass fraction on the walls ($j = c, e$)
Ω vorticity.

* Corresponding author. Tel.: 0049 9131 859486; fax: 0049 9131 859503; e-mail: alleborn@1stm.univ-erlangen.de

0017–9310/98/$—see front matter
PII: S0017–9310(98)00224–5

Subscripts
c cooled wall
e heated wall
i integer index
j index ($j = c, e$)
x, y vector components in x- and y-direction
0 steady configuration of flow, temperature and concentration fields
1 perturbation quantity
10 amplitude of the perturbation quantity.

1. Introduction

In drying technology detailed knowledge of the flow and of the heat and mass transfer in the drying chamber is essential for optimal operation of the equipment. In this paper, a type of idealized direct condensation dryer to be used for removing solvents from a thin liquid film on a moving web is modeled as a shallow cavity with two facing walls moving in their own planes and filled with a mixture of gas and solvent vapor. Heat is supplied to one moving wall in order to stimulate the evaporation of the liquid solvent. The other wall is cooled so that the solvent vapor in the cavity should condense on it. By moving the cooled wall, the condensed solvent can be removed from the cavity. The mass transport in the cavity is driven by diffusion due to the difference between the solvent vapor concentration near the heated and the cooled wall. It is influenced by convection induced by the motion of the walls and by thermal and solutal density changes. The impact of buoyancy on the flow depends on the orientation of the cavity in the gravity field, which can either oppose or support shear- and diffusion-induced convection. Overall, the driving mechanisms mentioned lead to complicated flow patterns in the cavity and strongly influence the heat and mass transfer rates (solvent evaporation rate) through the liquid film/gas interface in a drying chamber.

This problem of flow with moving surfaces, accompanied by heat and mass transfer, belongs to the family of lid-driven cavity problems already considered in the literature. However, it appears that only flow in a *driven* cavity accompanied by heat transfer has been studied thoroughly, and work on flow with heat *and* mass transfer problems has usually been focused on natural convection in enclosed cavities with *fixed* walls. A comprehensive understanding of the flow coupled with heat and mass transport processes in lid-driven cavities is still lacking.

A recent study by Kuhlmann et al. [1], devoted to two-dimensional flow in a rectangular cavity with the two short walls moving tangentially in opposite directions, refers to the first group of lid-driven cavity problems. In this paper multiple steady two-dimensional solutions were found for aspect ratios $L/H > 1.87$, with two co-rotating vortices present in the cavity at low Reynolds numbers. With increasing Reynolds number the flow pattern changes to a so-called cat's eye flow via two turning points eventually forming a single vortex flow at high Reynolds numbers.

An early paper by Batchelor [2] dealing with free convection heat transfer in a slot with differentially heated vertical walls was motivated by the application of double windows and thermal insulation of buildings. Different flow regimes were identified for limiting values of the Rayleigh number and the aspect ratio of the slot by asymptotic expansions for the solution of the governing equations. For a sufficiently tall cavity, such that the flow reaches fully developed conditions some distance away from the end walls, an aspect ratio was determined that gives minimal heat transfer depending on the Rayleigh number. Boundary layer theory and a Graetz–Nusselt procedure were applied in order to analyze the spreading of the temperature boundary layer into the fluid stream driven by free convection, and an estimate was given for the distance from either end of the cavity at which fully developed conditions are reached.

Iwatsu et al. [3] and Mohamad and Viskanta [4] investigated mixed convection in a square and in a shallow cavity with a stable vertical temperature gradient and with a moving upper lid of the cavity. Owing to the stable stratification of the fluid, the recirculation flow driven by the lid is confined to the upper region, whereas in the lower region heat transfer is dominated by conduction. Multicellular flow regimes and transition to three-dimensional flow were reported.

In a combined experimental and numerical study, Mansour and Viskanta [5] investigated mixed convection flow in a narrow vertical cavity, where one vertical wall is cooled and moves upwards, such that the shear forces induced by the wall motion oppose the buoyancy forces. For this case a slender vortex (shear cell) is observed to develop close to the moving wall while a buoyancy driven vortex occupies the remaining part of the cavity. The heat transfer rate between the two vertical walls becomes minimal when shear and buoyancy forces are of the same order of magnitude; it increases when either shear or buoyancy flow becomes dominant.

Papers dealing with combined heat and mass transfer focused on double diffusive natural convection in cavities with fixed walls. The work of Trevisan and Bejan [6] and of Bennacer and Gobin [7, 8] was concerned with heat and mass transfer in tall vertical cavities. From an analysis of the boundary layer regime, similarity solutions were derived and shown to compare well with numerical calculations over a wide range of parameters.

Dijkstra and Kranenborg [9] reported a comprehensive numerical study of double diffusive convection in a narrow slot with lateral temperature and concentration gradients. Using a continuation method, the steady two-dimensional flow configurations were

tracked in parameter space. The location of bifurcation points was detected and the linear stability of the solution branches was determined.

Whereas the aforementioned studies assumed a vanishing mass average fluid velocity at the walls, thereby neglecting an interaction of the flow field with the concentration gradients at the walls, this interaction was taken into account by appropriate boundary conditions in the work of Weaver and Viskanta [10] and of Ranganathan and Viskanta [11]. In their work, natural convection due to horizontal thermal and solutal gradients and the influence of diffusion on convection was considered.

In this work steady two-dimensional flow accompanied by heat and mass transfer in a shallow lid-driven cavity is investigated. The coupling between the velocity field and the concentration field at the evaporating or condensing wall is taken into account as well as buoyancy effects due to temperature gradients in the bulk of the fluid. A numerical continuation method is applied in order to trace the flow configurations in their dependence on the parameters of the system and to detect configuration multiplicities together with information on the linear stability of these configurations. Since, in drying applications, stable operating conditions with high mass transfer rates are desired, the influence of various operation parameters such as the Reynolds number, the relative velocities of the walls, and the buoyancy forces (Grashof number) on the heat and mass transfer rates is investigated here for several orientations of the cavity in the gravity field. For high differences in solvent concentration and low Reynolds numbers, a strong influence of convection induced by diffusion on the flow patterns is found. Depending on the orientation of the cavity, operation points with minimal heat and mass transfer as well as operation regimes with multiple flow configurations were detected in parameter space.

2. Problem formulation

A closed cavity with no through flow of height H and length L (see Fig. 1) filled with an ideal binary mixture of a solvent vapor and a non-condensable gas is considered. The heated wall, moving at velocity U_e, is kept at constant temperature T_e. It will be assumed that adjacent to the wall the solvent vapor mass fraction ω_e is also constant, corresponding to the equilibrium saturation. For the cooled wall constant values of T_c, ω_c and U_c are assumed similarly. The other two walls are considered adiabatic and impermeable. The fluid is treated as an incompressible, Newtonian fluid. Its density changes with temperature are taken into account by the Boussinesq approximation. Thermal diffusion (Dufour effect) and diffusion thermo (Soret effect) will not be considered. Finally, it will be assumed that the molar masses of the solvent and gas as well as their specific heats are equal, so that there is no density change with concentration and no interdiffusion effect.

Dimensionless quantities are introduced by scaling the lengths with the cavity height H and the velocities with the velocity of the heated wall U_e. The shape of the cavity is described by its aspect ratio

$$l = L/H \tag{1}$$

its orientation in the gravity field by the angle α (see Fig. 1). The physical properties of the fluid are characterized by the Prandtl number:

$$Pr = \frac{v}{\kappa} \tag{2}$$

and the Schmidt number:

$$Sc = \frac{v}{D} \tag{3}$$

defined in terms of the kinematic viscosity v, the thermal diffusivity κ and the diffusion coefficient D. The operation of the cavity is defined by a Reynolds number

$$Re = \frac{U_e H}{v} \tag{4}$$

the velocity ratio

$$u = U_c/U_e \tag{5}$$

and the Grashof number

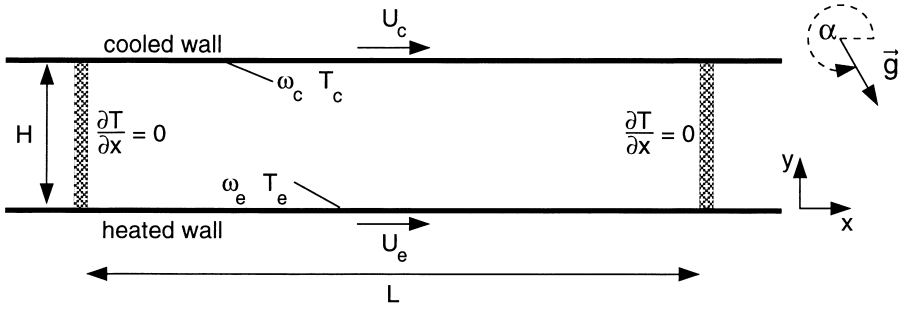

Fig. 1. Lid driven cavity, $g = g(\cos\alpha\, e_x + \sin\alpha\, e_y)$.

$$Gr = \frac{gH^3\beta_v(T_e - T_c)}{\nu^2} \tag{6}$$

where g denotes the gravitational acceleration and β_v the coefficient of thermal expansion. Gr can be viewed as a measure of the temperature difference as long as $\beta_v \neq 0$. Alternatively, it may be viewed as a measure of buoyancy influence. An additional parameter,

$$\Gamma = \frac{1-\omega_e}{\omega_e - \omega_c} \tag{7}$$

characterizes the concentration difference between the heated (subscript e) and cooled (subscript c) wall [10, 11].

With a streamfunction–vorticity approach for the two-dimensional velocity field,

$$u_x = \frac{\partial\psi}{\partial y}, \quad u_y = -\frac{\partial\psi}{\partial x} \tag{8}$$

and with normalized temperature and concentration fields

$$\nu = \frac{T - T_c}{T_e - T_c}, \quad C = \frac{\omega - \omega_c}{\omega_e - \omega_c} \tag{9}$$

the non-dimensional governing equations are given by [11, 12]:

- streamfunction equation:

$$\Delta\psi = \Omega \tag{10}$$

- vorticity transport:

$$\frac{\partial\psi}{\partial y}\frac{\partial\Omega}{\partial x} - \frac{\partial\psi}{\partial x}\frac{\partial\Omega}{\partial y} = \frac{1}{Re}\Delta\Omega - \frac{Gr}{Re^2}\left(g_x\frac{\partial\nu}{\partial y} - g_y\frac{\partial\nu}{\partial x}\right) \tag{11}$$

- heat transport:

$$\frac{\partial\psi}{\partial y}\frac{\partial\nu}{\partial x} - \frac{\partial\psi}{\partial x}\frac{\nu}{\partial y} = \frac{1}{RePr}\Delta\upsilon \tag{12}$$

- species mass transport:

$$\frac{\partial\psi}{\partial y}\frac{\partial C}{\partial x} - \frac{\partial\psi}{\partial x}\frac{\partial C}{\partial y} = \frac{1}{ReSc}\Delta C. \tag{13}$$

The boundary conditions are as follows: on the heated wall

$$\nu(x,0) = 1 \tag{14}$$

$$C(x,0) = 1 \tag{15}$$

$$\frac{\partial\psi}{\partial y}(x,0) = 1 \tag{16}$$

$$\frac{\partial\psi}{\partial x}(x,0) = \frac{1}{ReSc}\frac{1}{\Gamma}\frac{\partial C}{\partial y}(x,0) \tag{17}$$

and on the cooled wall

$$\vartheta(x,1) = 0, \tag{18}$$

$$C(x,1) = 0, \tag{19}$$

$$\frac{\partial\psi}{\partial y}(x,1) = u, \tag{20}$$

$$\frac{\partial\psi}{\partial x}(x,1) = \frac{1}{ReSc}\frac{1}{1+\Gamma}\frac{\partial C}{\partial y}(x,1). \tag{21}$$

Conditions (17) and (21), also known as Eckert–Schneider boundary conditions [13], couple the flow with diffusion. On the adiabatic and impermeable walls the conditions

$$\frac{\partial\nu}{\partial x}(0,y) = \frac{\partial\nu}{\partial x}(l,y) = 0 \tag{22}$$

$$\frac{\partial C}{\partial x}(0,y) = \frac{\partial C}{\partial x}(l,y) = 0 \tag{23}$$

hold for temperature and concentration. For the streamfunction

$$\psi(0,y) = 0 \tag{24}$$

$$\frac{\partial\psi}{\partial x}(0,y) = 0 \tag{25}$$

is set on one of these walls and

$$\psi(l,y) = \frac{1}{ReSc}\int_0^l \frac{1}{\Gamma}\frac{\partial C}{\partial y}(x',0)\,\mathrm{d}x' \tag{26}$$

$$\frac{\partial\psi}{\partial x}(l,y) = 0 \tag{27}$$

on the other. From the streamfunction equation (10) and from the conditions (16), (20), (25) and (27) at the four walls the boundary conditions for the vorticity are obtained [14].

Owing to the feedback of diffusion on the flow, the local heat and mass transfer coefficients h and k_ω, expressed by local Nusselt and Sherwood numbers

$$Nu_j(x) = \frac{hH}{\lambda} = -\left.\frac{\partial\upsilon}{\partial y}\right|_j \quad (j = c, e) \tag{28}$$

and

$$Sh_j(x) = \frac{k_\omega H}{D} = -\left.\frac{\partial C}{\partial y}\right|_j \quad (j = c, e) \tag{29}$$

respectively, depend on the mass transfer rate [15]. Their average values are defined by

$$\overline{Nu}_j = \frac{1}{l}\int_0^l Nu_j(x)\,\mathrm{d}x \tag{30}$$

and

$$\overline{Sh}_j = \frac{1}{l}\int_0^l Sh_j(x)\,\mathrm{d}x \tag{31}$$

respectively.

The dimensionless mass flux (per unit width) through the interfaces c and e for the unidirectional vapor diffusion is given by

$$M_e = \frac{\dot{m}_e}{\rho D/H} = \frac{1}{\Gamma}\overline{Sh}_e \tag{32}$$

and

$$M_c = \frac{\dot{m}_c}{\rho D/H} = \frac{1}{1+\Gamma}\overline{Sh}_c. \tag{33}$$

Since the other two walls are assumed to be impermeable, the global mass balance requires that

$$M_c = M_e. \tag{34}$$

Because of the Eckert–Schneider boundary conditions (17) and (21), a bulk flow contribution has to be added to the conductive heat flux Nu_j to give the total dimensionless heat flux through the walls:

$$\dot{Q}_j = \frac{\dot{q}_j}{\lambda(T_e - T_c)H} = \overline{Nu}_j + \frac{Pr}{Sc} v_j M_j. \tag{35}$$

The global energy balance for the cavity is given by

$$\overline{Nu}_c = \overline{Nu}_e + \frac{Pr}{Sc} M_e. \tag{36}$$

3. Numerical solution

The governing equations were discretized using a second-order finite difference scheme based upon an implementation of Alleborn et al. [12, 16]. The mesh was locally refined near the walls in order to resolve the wall boundary layers. An arc-length predictor–corrector continuation method by Allgower and Georg [17] was applied in order to track the solutions in dependence on the parameters and to detect turning points and simple bifurcation points. The numerical calculations were performed on a 150×30, a 150×60 and a 300×60 mesh. The global mass and energy balances (34) and (36), respectively, served as indicators for the numerical accuracy achieved. On the finest grid (300×60 points) the relative error for both mass and energy balance was below 0.05% in the range of parameters investigated. The differences of both averaged Nusselt and Sherwood numbers between the two finest grids was well below 0.5%. Furthermore, the results of this algorithm were compared with the results of Mansour and Viskanta [5] for laminar flow in a shallow cavity with aspect ratio $l = 6$ and with the results of Ranganathan and Viskanta [11] for natural convection with mass transfer in a square cavity. For both cases the relative deviation of our numerical results was less than 3%.

For the computed steady configurations of flow, temperature and concentration fields $(\psi_0, \Omega_0, v_0, C_0)\ (x, y)$, the linear stability with respect to two-dimensional disturbances $(\psi_1, \Omega_1, v_1, C_1)\ (t, x, y)$ was determined. The governing equations for the perturbed flow

$$\tilde{\psi}(t, x, y) = \psi_0(x, y) + \psi_1(t, x, y) \tag{37}$$

$$\tilde{\Omega}(t, x, y) = \Omega_0(x, y) + \Omega_1(t, x, y) \tag{38}$$

$$\tilde{v}(t, x, y) = v_0(x, y) + v_1(t, x, y) \tag{39}$$

$$\tilde{C}(t, x, y) = C_0(x, y) + C_1(t, x, y) \tag{40}$$

were linearized with respect to the perturbation quantities and solved by a normal mode decomposition

$$(\psi_1, \Omega_1, v_1, C_1)(t, x, y) = (\psi_{10}, \Omega_{10}, v_{10}, C_{10})(x, y)e^{\sigma t} \tag{41}$$

with a complex growth rate σ. The generalized algebraic eigenvalue problem for σ resulting from discretization was solved with the package ARPACK [18]. Both continuation method and linear stability analysis had already been used in previous work [12]. Figure 2 shows as an illustration the grid dependence of the dominant part of the spectrum for a particular parameter configuration at $Re = 1000$. The right-most eigenvalues are situated in the left half of the complex plane, i.e. small perturbations decay with time and the basic flow is stable. To a good approximation this part of the spectrum is independent of the grid size. Owing to the increase in the number of degrees of freedom with increasing number of grid points, the inner part of the spectrum changes with grid refinement, as expected.

4. Limiting cases

4.1. One-dimensional model

In the limiting case of an infinitely long cavity, $l \to \infty$, and with negligible buoyancy forces, an analytical solution can be obtained for fully developed flow [13]. From conservation of mass and from the Eckert–Schneider boundary conditions (17), a constant velocity component in the y-direction follows:

$$v = \frac{1}{ReSc} \log \frac{1+\Gamma}{\Gamma}. \tag{42}$$

In terms of the constant vertical velocity v, the concentration profile is given by

$$C(y) = \frac{e^{vReSc} - e^{vReScy}}{e^{vReSc} - 1}. \tag{43}$$

The corresponding temperature profile can be obtained from equation (43) by replacing C by v and Sc by Pr.

In Fig. 3, the analytical concentration profile for $l \to \infty$ is compared with the numerical profiles in the middle ($x = 2.5$) of a cavity of finite length ($l = 5$), for low Reynolds number and for different values of Γ. For low Re, Pr and Sc, the flow in a finite cavity can be considered fully developed already close to the end walls in cavities with finite length. In this region good agreement between the two-dimensional simulation and the analytical solution is found.

Figure 4 shows in detail the numerical solution for a cavity with finite length $l = 5$ and the upper and lower wall moving in opposite directions ($u = -1$) at $Re = 10$, referred to in Fig. 3. Buoyancy was neglected in this calculation ($Gr = 0$). For low Reynolds numbers and

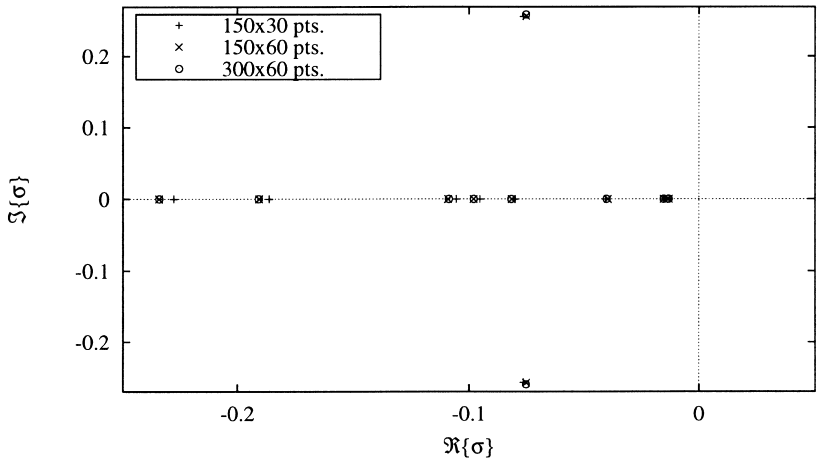

Fig. 2. Grid dependence of the right-most eigenvalues of the spectrum for $l = 5$, $Pr = 0.85$, $Sc = 0.56$, $Re = 1000$, $Gr = 0$, $u = -1$, $\Gamma = 0.334$.

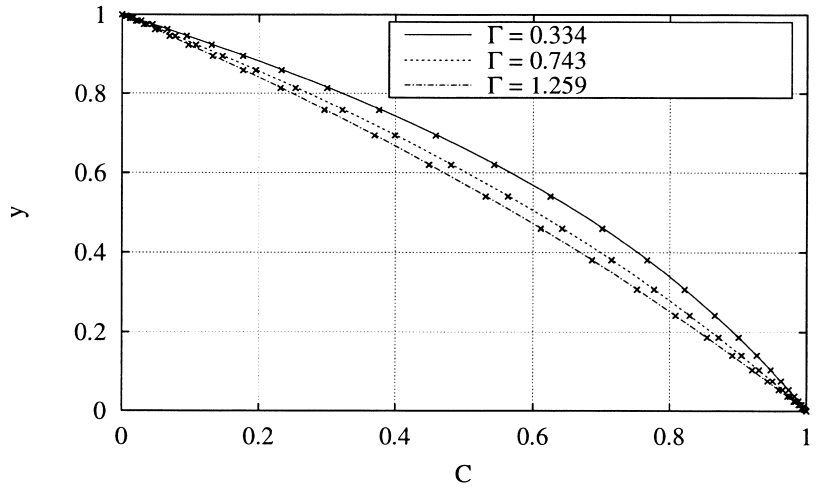

Fig. 3. Concentration profiles in the drying chamber at $x = 2.5$ for $l = 5$ at $Re = 10$, $Sc = 0.56$ ($Pr = 0.85$, $Gr = 0$ and $u = -1$): $\times$ numerical results, — analytical solution.

high concentration gradients, the fluid motion is strongly influenced by diffusion-induced convection. The convection cell which would occupy the whole cavity if the diffusion flux were negligibly small is squeezed into the left part of the cavity by the strong mass flux from the heated (evaporating) to the cooled (condensing) wall (see Fig. 4). The temperature and concentration contour lines are approximately horizontal in the mid-part of the cavity and slightly distorted by convection near the adiabatic end walls. In Fig. 4 the local Nusselt numbers for the one-dimensional analytical model are plotted together with the numerical results, showing the region in the cavity with fully developed flow.

With increasing Reynolds number, the shear-induced fluid motion becomes dominant and the recirculation cell increases in size, occupying the central part of the cavity (Fig. 5). Even at higher Reynolds numbers, however, the influence of diffusion-induced convection distorts the shape of the recirculation cell which would have a perfect central symmetry in the absence of diffusion.

In the core of the convection cell the temperature and concentration are approximately constant. Close to the moving lids boundary layers of temperature and concentration develop in the direction of the wall motion. Batchelor [2] used the Graetz–Nusselt procedure to analyze the spreading of the thermal boundary layer in the

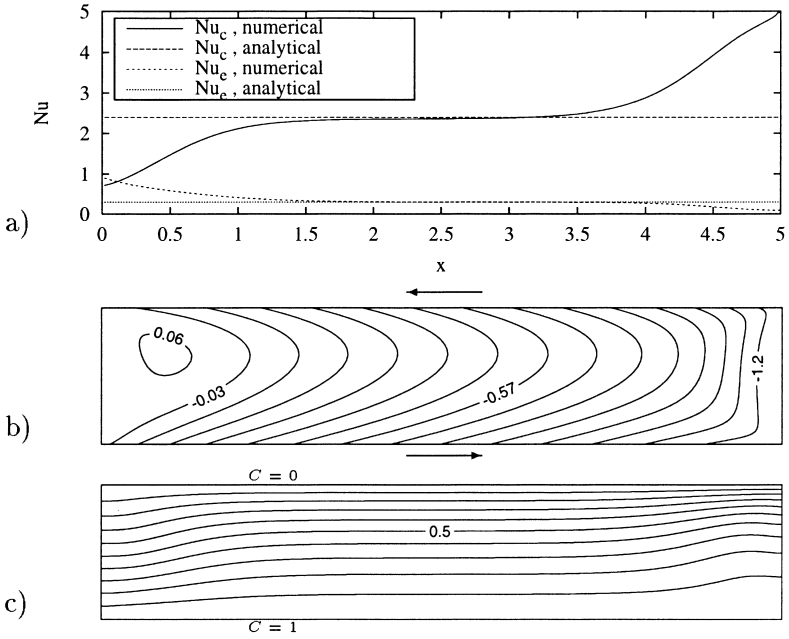

Fig. 4. Local Nusselt numbers (a), streamlines (b) and concentration contours (c) for $l = 5$, $Re = 10$, $Pr = 0.85$, $Sc = 0.56$, $u = -1$, $Gr = 0$, $\Gamma = 0.334$.

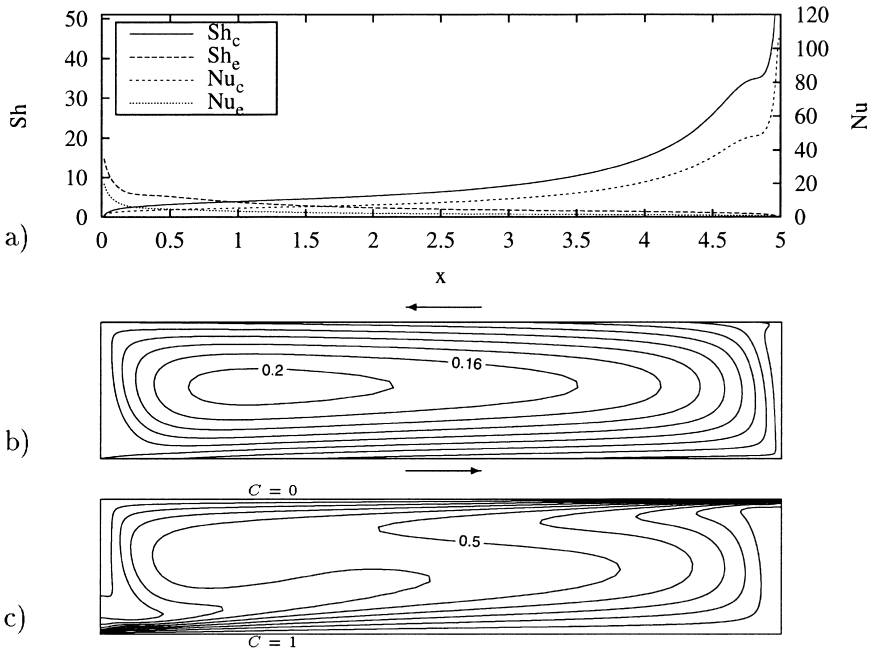

Fig. 5. Local Nusselt and Sherwood numbers (a), streamlines (b) and concentration contours (c) for $Re = 500$, $u = -1$, $Gr = 0$, $\Gamma = 0.334$.

case of free convection in a vertical slot. In the following section the method will be adapted to solve the Graetz–Nusselt problem for forced convection flow in the driven cavity.

4.2. Thermal boundary layer

The flow profile in a long, shallow cavity with its long walls moving in opposite directions ($u = -1$) can be described approximately by a fully developed Couette profile some distance away from the end walls. At high Reynolds numbers and for moderate and high Prandtl numbers thin thermal boundary layers develop along the moving walls while the fluid in the core of the cavity is nearly isothermal. The temperature boundary layer equation for a Couette profile

$$(1-2y)\frac{\partial v}{\partial x} = \frac{1}{RePr}\frac{\partial^2 v}{\partial y^2} \tag{44}$$

is solved for the temperature boundary condition at the lower moving wall

$$v(x,0) = 1 \tag{45}$$

and constant temperature at the horizontal centerline of the cavity

$$v(x,1/2) = \frac{1}{2}. \tag{46}$$

At $x = 0$ a constant temperature

$$v(0,y) = \frac{1}{2} \tag{47}$$

will be assumed as well.

The problem is solved by separation of variables; the general solution is given by

$$v(x,y) = (1-y) + \sum_{i=1}^{\infty} a_i \, \mathrm{e}^{-\frac{\lambda_i}{2Pe}x}\phi_i(y), \tag{48}$$

with Peclet number $Pe = RePr$. The functions $\phi_i(y)$ form a complete set of orthonormal functions which are obtained from a power series solution of the Sturm–Liouville problem resulting from the separation ansatz for equation (44). The corresponding eigenvalues λ_i are determined form the boundary conditions (45) and (46). Approximations for the first ten eigenpairs (λ_i, $\phi_i(y)$) are obtained by the computer algebra program MAPLE, the first five eigenvalues are determined as

$$\lambda_i \approx 151.65, 655.09, 1513.77, 2727.74, 4297.01, \ldots \tag{49}$$

The coefficients a_i in equation (48) are obtained from the initial condition (47) by orthogonal projection. For $x \to \infty$ the solution (48) tends asymptotically to the linear temperature profile of the fully developed solution. The rate at which the deviation of the fully developed profile decreases with x will be asymptotically determined by the first term ($i = 1$) of the series expansion in equation (48) [2]. The distance for which this term decreases to 10% of its initial value gives a rough estimate of the distance x_d from the vertical end walls for which flow and temperature fields can be considered fully developed:

$$x_d \approx \frac{Pe}{33}. \tag{50}$$

In Fig. 6, the local Nusselt numbers obtained from a numerical solution for a cavity with parameters $l = 10$, $Re = 3000$, $Pr = 2$, $Gr = 0$, without mass transfer, are compared with the analytical approximation

$$Nu_{\text{analyt}} = 1 - \sum_{i=1}^{10} a_i \, \mathrm{e}^{-\frac{\lambda_i}{2Pe}x}\phi_i'(0) \tag{51}$$

for $Pe = 6000$.

In the first case (dotted line in Fig. 6), the initial condition (47) is used. Since the flow driven by the lids is turned around by the vertical end walls and reaches into the core of the cavity, the assumption of constant temperature in equation (47) appears not to be a very good approximation of the temperature profile near the end walls. However, since the rate at which the temperature profile reaches the linear profile as x increases is determined very soon only by the first term in equation (48), the particular shape of the temperature profile at $x = 0$ very rapidly becomes unimportant with growing x. Therefore, the analytical solution for the local Nusselt number for constant initial condition can be reasonably fitted to the numerical result by shifting it by a constant length x_v, which is similar in concept to the virtual origin of a Bickley jet [13]. Figure 6 shows that the rate at which the Nusselt numbers decreases with x compares well with the numerically obtained results. Even better agreement for the asymptotic behavior of Nu was obtained by using a numerically obtained temperature profile near the left end wall ($x = 0.69$) instead of equation (47) as an initial condition (dashed line in Fig. 6).

5. Numerical study

In the general case of a finite cavity length and arbitrary operation parameters, a numerical simulation of the transport processes is necessary. In this paper a cavity with aspect ratio $l = 5$ is considered. For the solvent vapor/gas mixture the Prandtl and Schmidt numbers

$$Pr = 0.85 \tag{52}$$

$$Sc = 0.56 \tag{53}$$

were chosen.

Four different orientations of the cavity in the gravity field were selected for the parameter study:

(i) vertical cavity with the heated wall moving upwards ($\mathbf{g} = -g\mathbf{e}_x$, $\alpha = 180°$);
(ii) vertical cavity with the heated wall moving downwards ($\mathbf{g} = +g\mathbf{e}_x$, $\alpha = 0°$);

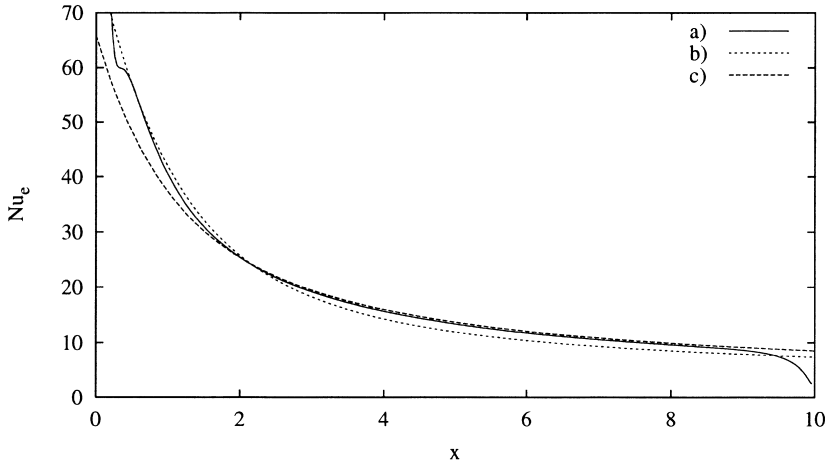

Fig. 6. Local Nusselt number Nu vs x. (a) Numerical solution ($Pe = 6000$, $l = 10$); (b) Graetz–Nusselt solution with constant initial temperature $v(0, y) = 1/2$, virtual origin: $x \to x - x_v$; (c) Graetz–Nusselt solution, numerically obtained profile ($Pe = 6000$) at $x_n = 0.69$ as initial condition $v(x_n, y)$.

(iii) horizontal cavity with heated lower lid ($\mathbf{g} = -g\mathbf{e}_y$, $\alpha = 270^\circ$);
(iv) horizontal cavity with heated upper lid ($\mathbf{g} = +g\mathbf{e}_y$, $\alpha = 90^\circ$).

5.1. Influence of the Reynolds number

The dependence of heat and mass transport on the Reynolds number is shown in Fig. 7(a) and (b) in terms of average Nusselt and Sherwood numbers for the walls moving in opposite directions ($u = -1$). The calculations were performed for four cavity orientations, with a concentration parameter $\Gamma = 0.334$, corresponding to saturation mass fractions of water vapor (1 bar) at $T_e = 368$ K and $T_c = 293$ K, and with $\Gamma = 1.259$, corresponding to saturation at $T_e = 358$ K and $T_c = 293$ K. Figure 7(b) shows a drastic increase of the mass transfer with an increase of about 10 K in the evaporation temperature, but a qualitatively similar behavior of the heat and mass transfer rate with the remaining operation parameters for both $\Gamma = 0.334$ and $\Gamma = 1.259$.

The results show that for $Re > 350$, heat and mass transfer is dominated by convection driven by the moving lids. Buoyancy forces have practically no influence on the heat and mass transfer rate, so that the Nusselt and Sherwood numbers do not depend significantly on the orientation of the cavity (cases (i)–(iv)). The typical flow pattern in this range of Reynolds numbers is a single vortex. In conjunction with it, temperature and concentration boundary layers develop near the lids whereas the core of this vortex is almost isothermal and with constant vapour concentration (Fig. 5).

At $Re < 350$ there is a regime of mixed convection where viscous forces and buoyancy forces are competing. In Fig. 8 a magnification of the range of Reynolds numbers covering the mixed convection regime is plotted for $Gr = 7785$ and $\Gamma = 0.334$. The extreme heat and mass transfer rates are attained here for a vertical cavity: the highest rates with the heated lid moving upwards (case (i), $\alpha = 180^\circ$, solid line), and the lowest ones for the heated lid moving downwards (case (ii), $\alpha = 0^\circ$, dot-dashed line in Fig. 8).

For case (i), with upward-moving heated lid the buoyancy forces in the fluid act in the same direction as the shear forces of the moving walls. Hence the convective transport of solvent vapor from the heated wall to the cooled wall is enhanced, resulting in the higher heat and mass transfer rates.

When, in contrast, the heated lid moves downwards (case (ii)), the buoyancy forces oppose the shear forces, thus increasing the thicknesses of the temperature and concentration boundary layers and decreasing the heat and mass transfer rates.

Figure 9(a) and (b) compares the streamlines and contour lines of concentration of these two cases at $Re = 150$. In addition, Fig. 10 shows for these two cases the velocity and concentration profiles across the cavity at $x = 2.5$. They confirm the smaller velocities in the cavity for opposing buoyancy and shear. Owing to the decelerating action of the buoyancy forces, the center of the recirculation zone is shifted in case (ii) to the upper end of the cavity whereas in the core of the cavity the fluid is moving slowly (see Fig. 9 and dashed line in Fig. 10), so that heat and mass transport are dominated here by

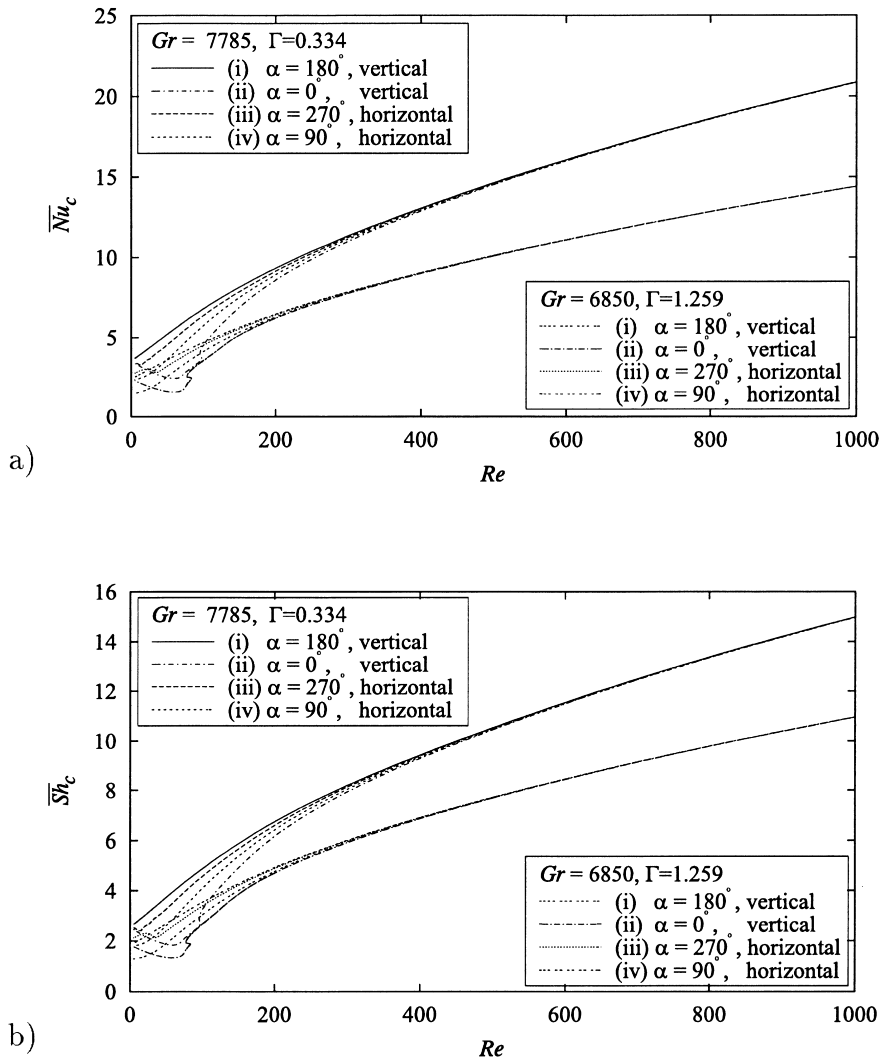

Fig. 7. Influence of the Reynolds number and the orientation of the cavity on heat and mass transfer for $l = 5$, $Pr = 0.85$, $Sc = 0.56$, $u = -1$: (a) heat flux: average Nusselt number, (b) mass flux: average Sherwood number.

diffusion. With concurring buoyancy and shear, concentration gradients at the walls are significantly steeper (Fig. 10), so that heat and mass transport in case (i) take place dominantly in the boundary layers.

When the Reynolds number is decreased still further below $Re = 150$, the heat and mass transfer rates decrease in a simple monotonic way in case (i) whereas in case (ii) the dependence of the Nusselt and Sherwood numbers on the Reynolds number displays a more complicated behavior. A threefold flow configuration appears here, that lies for $\Gamma = 0.334$ between $Re = 94.69$ and $Re = 96.78$, and is limited in the diagram of Fig. 8 by two turning points. The flow configuration corresponding to the branch between the two turning points turns out to be unstable. It exhibits two additional vortices, compared to the stable flows above the turning point at $Re = 94.69$ (Fig. 11(a)), and is qualitatively similar to the flow configuration at the turning point at $Re = 96.78$ (Fig. 11(b)). For $\Gamma = 1.259$ this region of threefold flow configurations is located between $Re = 77.26$ and 83.34, respectively.

At $Re \approx 60$, buoyancy forces and viscous forces counteract each other in such a way as to produce a flow (Fig. 12) with minimal heat and mass transfer rates (cf. Fig. 7(a) and (b)). On decreasing the Reynolds number still further, the buoyancy forces eventually dominate the

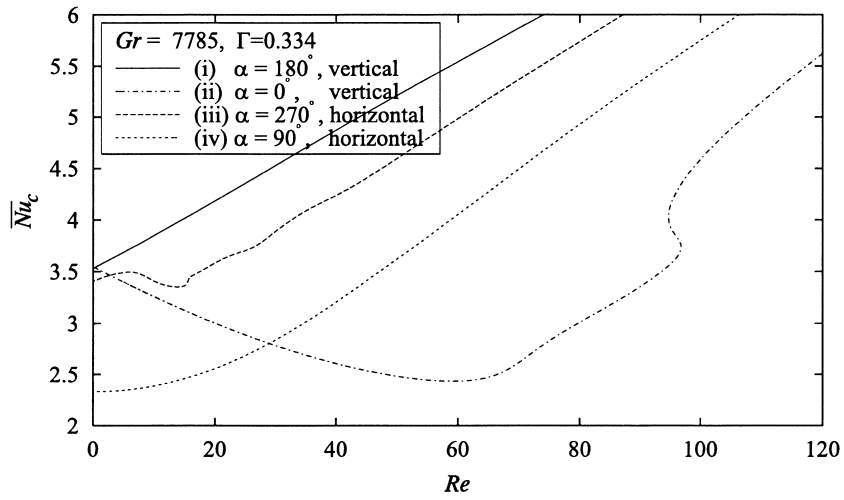

Fig. 8. Heat flux (dimensionless) vs Reynolds number: magnified plot of mixed convection regime for $Gr = 7785$, $\Gamma = 0.334$, $l = 5$, $Pr = 0.85$, $Sc = 0.56$, $u = -1$.

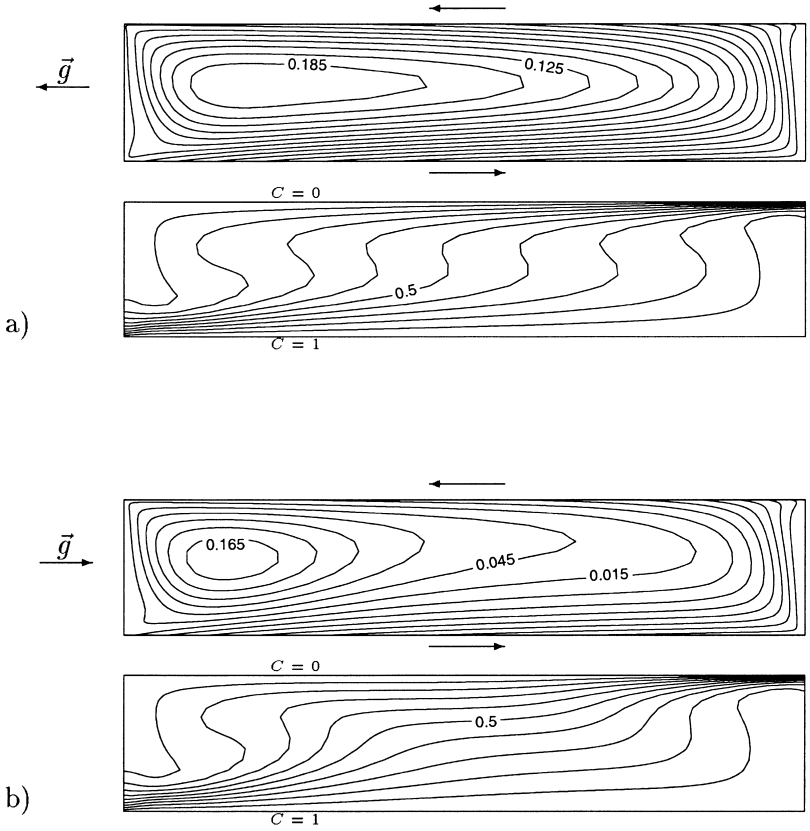

Fig. 9. Streamlines and concentration contours for $Gr = 7785$, $l = 5$, $Re = 150$, $Pr = 0.85$, $Sc = 0.56$, $u = -1$, $\Gamma = 0.334$: (a) $\alpha = 180^\circ$, heated wall moving upwards (b) $\alpha = 0^\circ$, heated wall moving downwards.

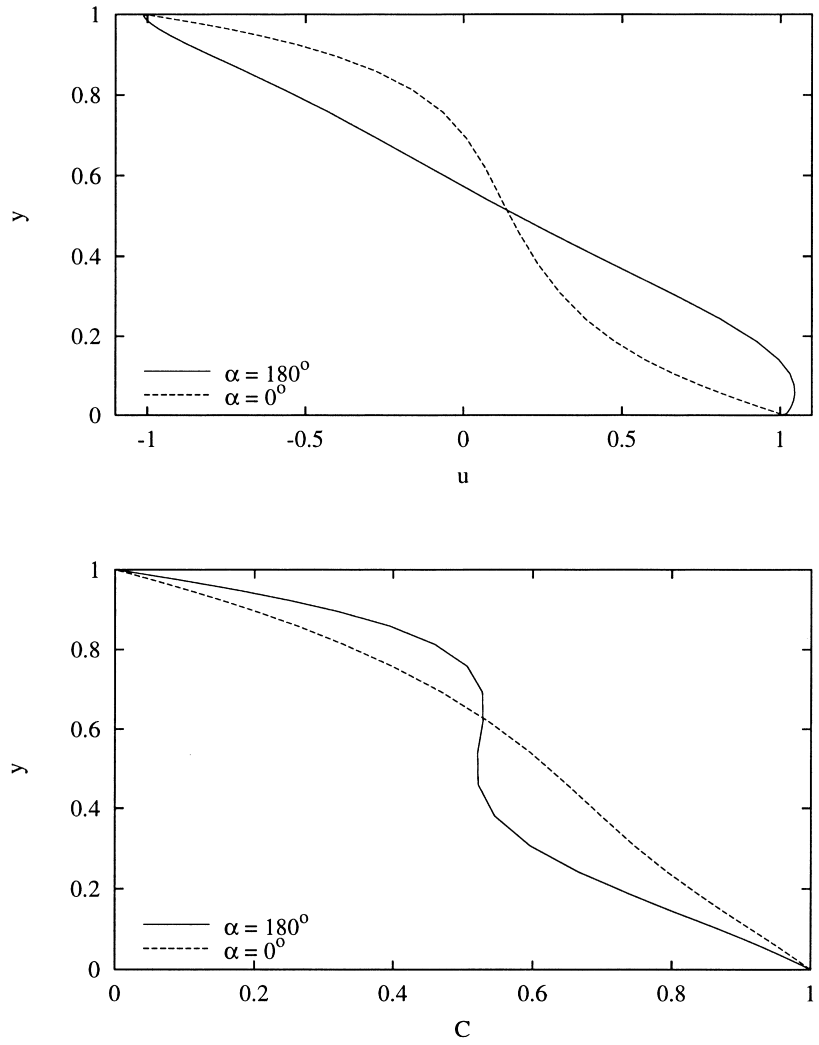

Fig. 10. Velocity profile (u-component, upper diagram) and concentration profile (lower diagram) at $x = 2.5$, for $Gr = 7785$, $l = 5$, $Re = 150$, $Pr = 0.85$, $Sc = 0.56$, $u = -1$, $\Gamma = 0.334$.

flow and produce a flow pattern as shown in Fig. 13. In this flow the vortex rotates clockwise, opposite to the anti-clockwise rotation of the vortices in Figs 5 and 9. The heat and mass transfer rates increase again and reach the rates of case (i) in the limit $Re \to 0$ of fixed walls.

For the horizontal cavities the values of the heat and mass transfer rates lie between those for vertical cavities. For a stable stratification of the vapor/gas mixture, i.e. for the lower wall cooled and the upper wall heated ($\alpha = 90^\circ$), lighter fluid tends to oppose at low Reynolds numbers the convection down to the cool wall. Therefore, the vortex appears confined to a narrow region close to the upper wall (Fig. 14). With decreasing Reynolds number a second vortex develops in the cold, heavy fluid layer near the bottom lid. In the limit $Re \to 0$, heat and mass transfer become mainly driven by diffusion-induced convection.

For an unstable stratification, with the cooled lid located above the heated one ($\alpha = 270^\circ$), the buoyancy forces support the convective transport of the fluid away from the moving lids. With decreasing Reynolds number the buoyancy forces gain dominance over the shear-driven flow. As a consequence, at $Re \approx 43$ the single vortex flow of the forced convection regime (Fig. 5) starts to divide into two anti-clockwise rotating vortices. At $Re = 30.016$ this steady two-dimensional flow pattern

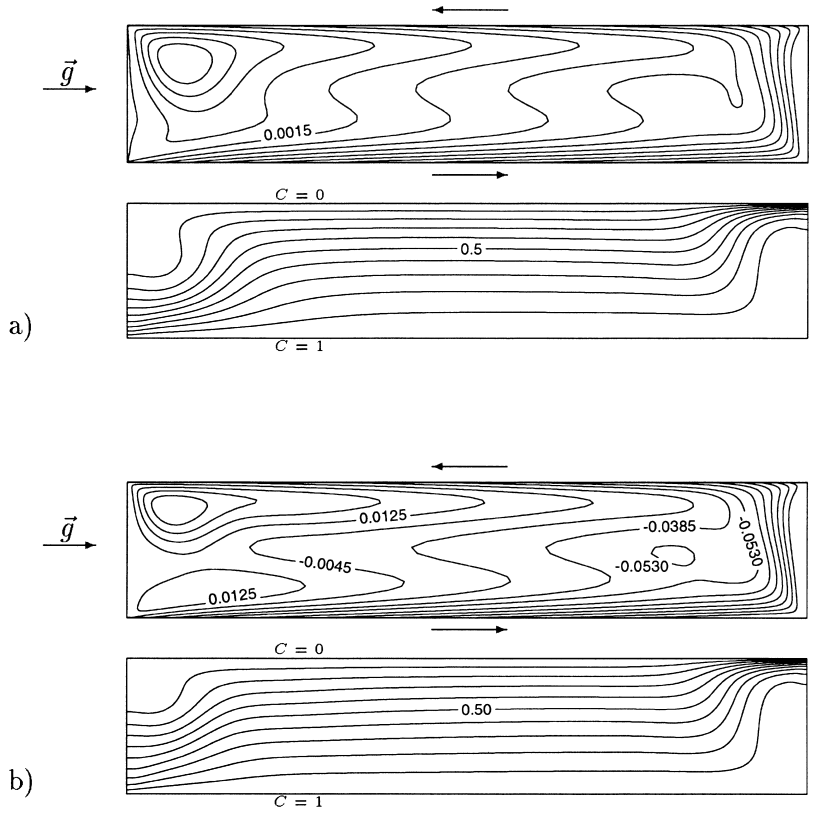

Fig. 11. Streamlines and concentration contours at critical points for $Gr = 7785$, $\alpha = 0^\circ$, $u = -1$, $\Gamma = 0.334$: (a) first turning point at $Re = 94.69$, (b) second turning point at $Re = 96.78$.

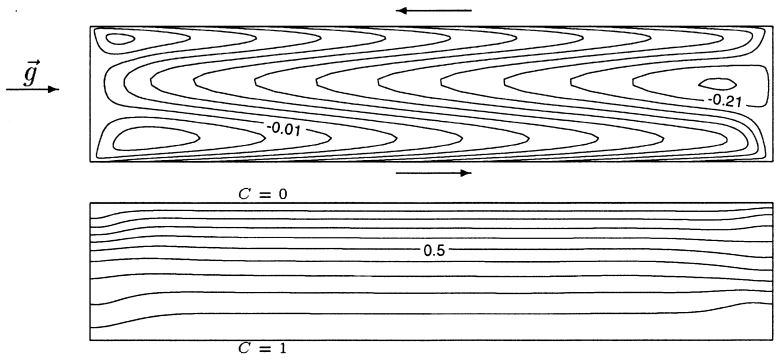

Fig. 12. Minimal heat and mass transfer at $Re = 60$ for $Gr = 7785$, $\alpha = 0^\circ$, $u = -1$, $\Gamma = 0.334$.

(Fig. 15) becomes unstable with respect to two-dimensional disturbances by a Hopf bifurcation and transient behavior sets in. This transition is shown by the rightmost part of the spectrum of linear stability at the bifurcation point $Re = 30.016$ in Fig. 16. A pair of complex conjugate eigenvalues crosses from the left to the right half of the

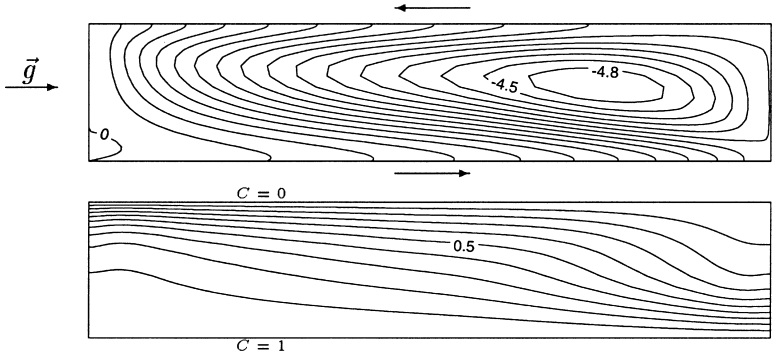

Fig. 13. Buoyancy dominated flow, shown for $Re = 5$, $Gr = 7785$, $\alpha = 0^\circ$, $u = -1$, $\Gamma = 0.334$.

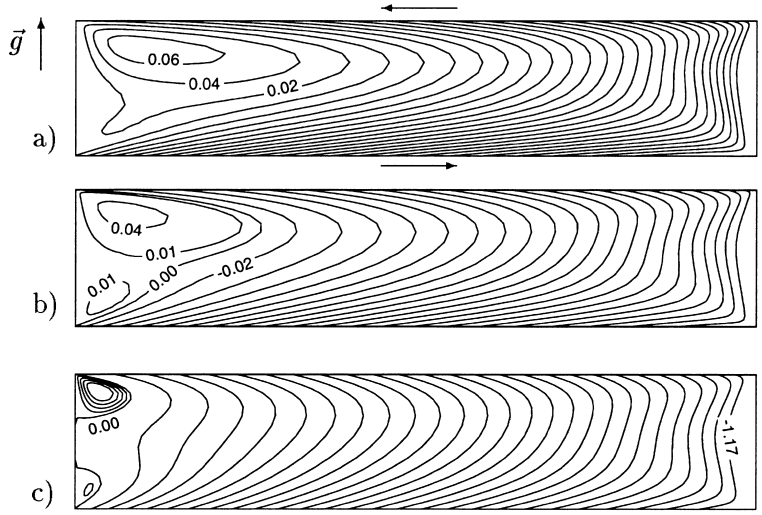

Fig. 14. Streamlines for a horizontal cavity, stable stratification. (a) $Re = 30$, (b) $Re = 20$, (c) $Re = 10$, for $l = 5$, $Pr = 0.85$, $Sc = 0.56$, $Gr = 7785$, $\alpha = 90^\circ$, $u = -1$.

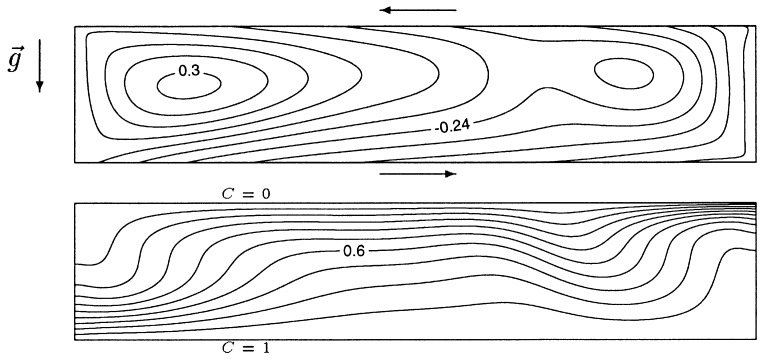

Fig. 15. Horizontal cavity, streamlines and concentration contours at $Re = 30.016$ (Hopf point) for $l = 5$, $Pr = 0.85$, $Sc = 0.56$, $Gr = 7785$, $\alpha = 270^\circ$, $u = -1$, $\Gamma = 0.334$.

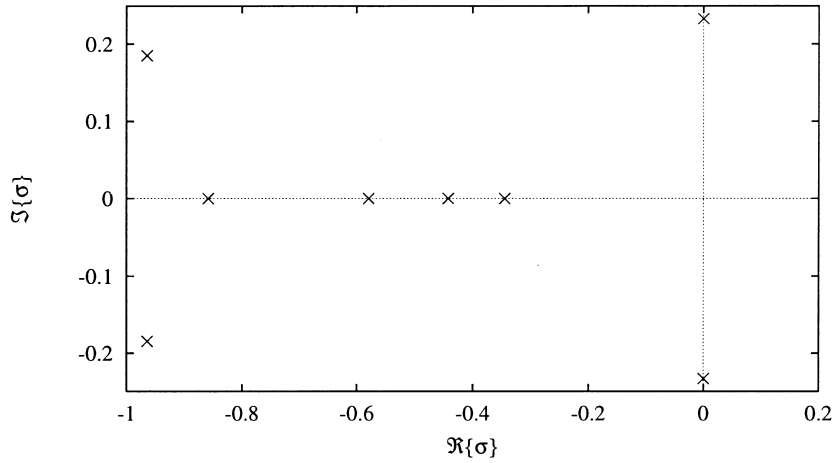

Fig. 16. Hopf bifurcation: right-most eigenvalues of the stability spectrum for $Re = 30.016$, $l = 5$, $Pr = 0.85$, $Sc = 0.56$, $Gr = 7785$, $u = -1$, $\Gamma = 0.334$.

complex plane. Close to the Hopf bifurcation point the transient flow is periodic with an angular frequency $\Im\{\sigma\} \approx 0.23$.

5.2. *Influence of the velocity ratio* u

When the cavity is operated in the forced convection regime at a fixed Reynolds number, the relative velocity of the moving lids can strongly influence the heat and mass transport. Figure 17(a) and (b) shows for $Re = 500$ that the heat and mass transfer rates decrease drastically when the relative velocity of the condensing wall is changed from $u = -1$ to $u = 1$. This decrease is most pronounced in the range of a relatively slowly moving cooled lid ($-0.5 < u < 0.5$) where also slight influence of the buoyancy force can be observed. Similarly to the findings in the previous section, the qualitative behavior of the heat and mass transfer with the velocity ratio u and cavity orientation in the gravity field does not depend on the concentration level Γ.

Figures 5 and 18(a)–(f) show the change of the flow and concentration field for $\Gamma = 0.334$ when the velocity ratio u changes from -1 to 1. When the velocity of the cooled lid (upper lid in the figures) is decreased from $u = -1$ to $u = -0.5$ (Fig. 18(a)), the fluid accelerated by the faster heated lid (lower lid in the figures), is decelerated by the slower motion of the cooled lid. The center of the core vortex is shifted from the left to the middle of the cavity and hot fluid, rich in solvent, reaches deeper into the core. With a further decrease in the speed of the cooled wall, separation occurs on the upper wall, with the consequence that the recirculation zone in the cavity decreases in size and two new vortices develop as u tends to zero (Fig. 18(b) and (c)). Outside the major vortex the fluid velocity is so small that the heat and mass transport is driven mainly by diffusion and does not contribute much to the total heat and mass transfer. Therefore, the onset of separation on the cooled wall explains the steep decrease of the heat and mass transfer rates for $u > -0.5$.

Motion of the cooled lid in the direction of the heated lid leads to the development of a complex flow pattern: in the upper and lower halves of the cavity there appear arrays of co-rotating vortices (Fig. 18(d)–(f)). Thereby, the upper vortex array rotates oppositely to the lower array. Between them a narrow fluid jet undulates in a flow opposed to the motion of the walls. Owing to the convective mixing produced by the vortices, the temperature and concentration gradients near the moving walls are leveled and lead to lower heat and mass transfer rates compared with the flow with oppositely moving walls. For $u \approx 0.6$ shallow minima are reached by the heat and mass transfer rates, followed by a slow increase at $u > 0.6$ (Fig. 17), when the cooled wall moves fast enough to build up a thin boundary layer over its entire length (Fig. 18(f)).

It is instructive to trace the path of a fluid element of the vapor/gas mixture from the evaporation wall to the condensation wall: Solvent vapor emerging from the heated lid first diffuses into a fluid element close to it, thereby increasing its mass fraction of solvent vapor. For $u > 0$ this fluid element is transported typically on an S-shaped trajectory that passes through the undulating fluid stream in the middle of the cavity (see Fig. 18(d)–(f)) to the cool wall where its vapor content condenses. On this way the fluid element loses part of its vapor content by diffusion. For $u < 0$, on the contrary, the typical trajectory of a fluid element is considerably shorter, because after its first turn near the right end wall it arrives very close to the cool wall, keeping its high solvent vapor concentration (see Fig. 5). Therefore, approximately

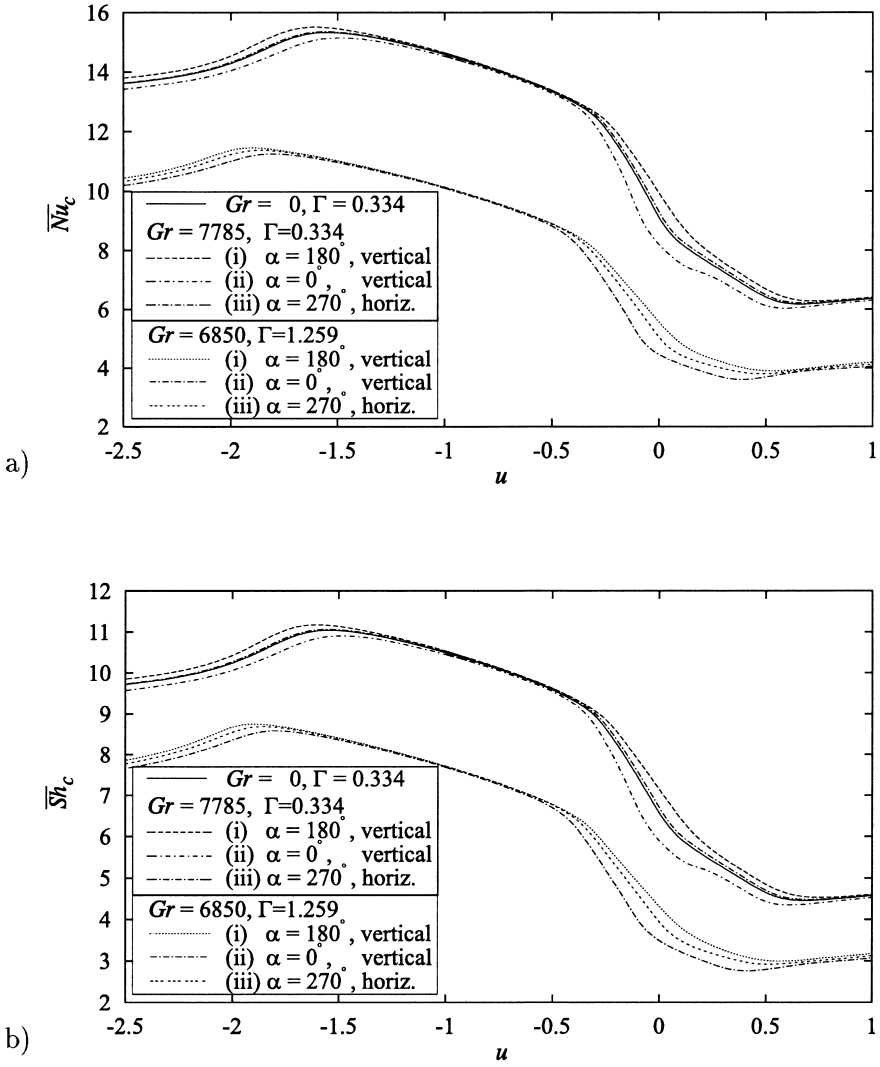

Fig. 17. Influence of the velocity ratio u and the orientation of the cavity on heat and mass transfer for $Re = 500$, $l = 5$, $Pr = 0.85$, $Sc = 0.56$: (a) heat flux: average Nusselt number, (b) mass flux: average Sherwood number.

twice as much solvent vapor is transported here to the cooled wall and condenses there, leading to considerably higher heat and mass transfer rates.

When the cooled wall moves in the opposite direction and faster than the heated wall ($u < -1$), the heat and mass transfer rates (Fig. 17(a) and (b)) increase slightly and reach a local maximum (around $u = -1.6$ for $\Gamma = 0.334$). The flow pattern at this maximum (Fig. 19(a)) is similar to that shown in Fig. 5 for $u = -1$, but the temperature and concentration in the core of the vortex are lower for the faster moving cooled wall. Furthermore, the cold fluid that is turned around at the left end wall has a higher momentum when it impinges on the heated wall. This results in locally thinner temperature and concentration boundary layers and leads to higher local heat and mass transfer rates.

When the velocity of the cooled belt is further increased, flow separation occurs for $u < -1.6$ on the slower heated wall and influences the overall heat and mass transfer rates. The size of the core vortex decreases and its center shifts towards the left end wall (cf. Fig. 19(b)). The temperature and concentration in the vortex are almost constant and very close to their values right on the cooled wall. Therefore, cold fluid is convected close to the heated wall and heat and mass transfer are enhanced here. Outside the vortex, beyond the separation point, the fluid velocity is comparatively small, leading to considerably lower local heat and mass transfer rates

on the heated lid than for $u \approx -1.6$. Because of the size of this zone compared to the vortex, the average heat and mass transfer rates are decreased significantly.

For the situation of a faster moving cooled wall the heat and mass transfer rates show some dependence on the orientation of the cavity in the gravity field, similar to a slower moving cooled wall, because in the zones of slow fluid motion, outside the core vortex, buoyancy forces gain a noticeable influence compared with the shear forces. Figure 17(a) and (b) displays this; again, the effect is most pronounced for vertical cavities, for the same reasons as described in Section 5.1.

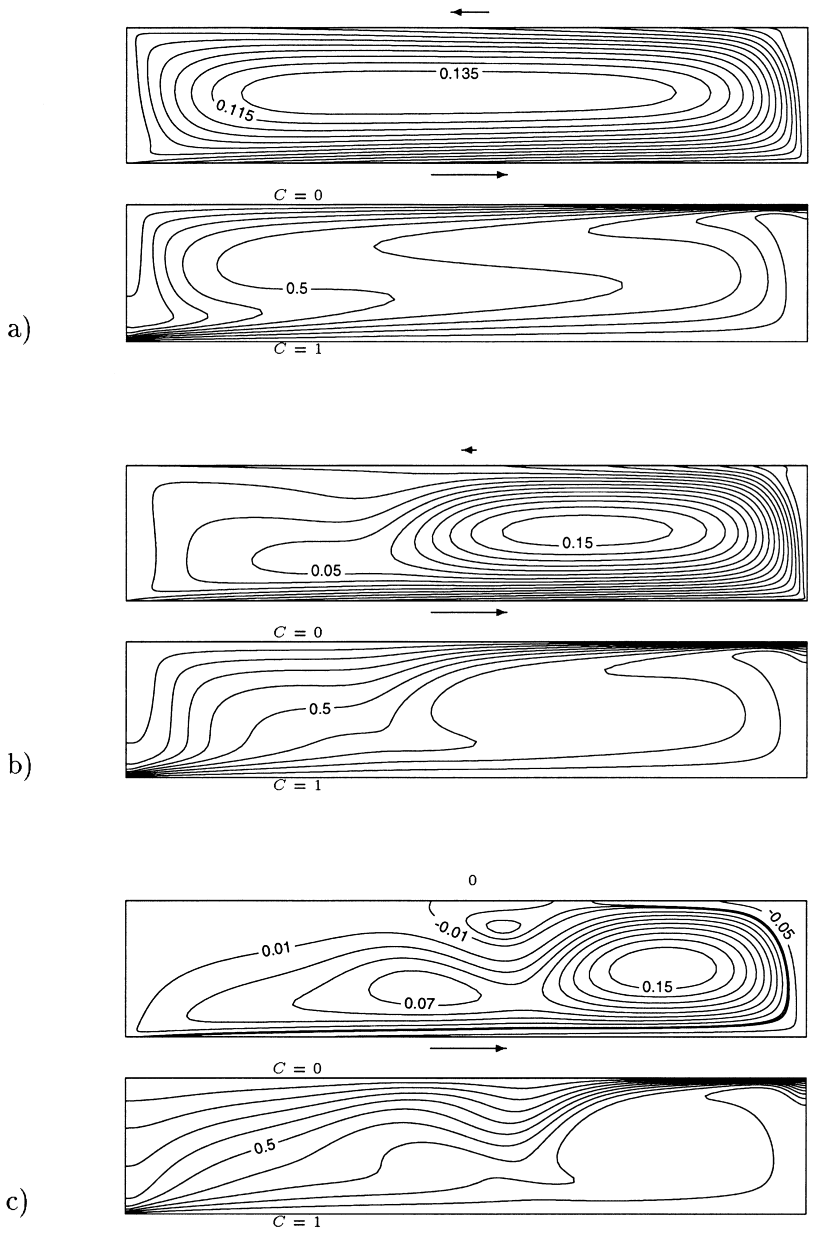

Fig. 18. Influence of the velocity ratio u on flow and concentration field for $l = 5$, $Re = 500$, $Pr = 0.85$, $Sc = 0.56$, $Gr = 0$, $\Gamma = 0.334$: (a) $u = -0.5$, (b) $u = -0.2$, (c) $u = 0$, (d) $u = 0.2$, (e) $u = 0.5$, (f) $u = 1$.

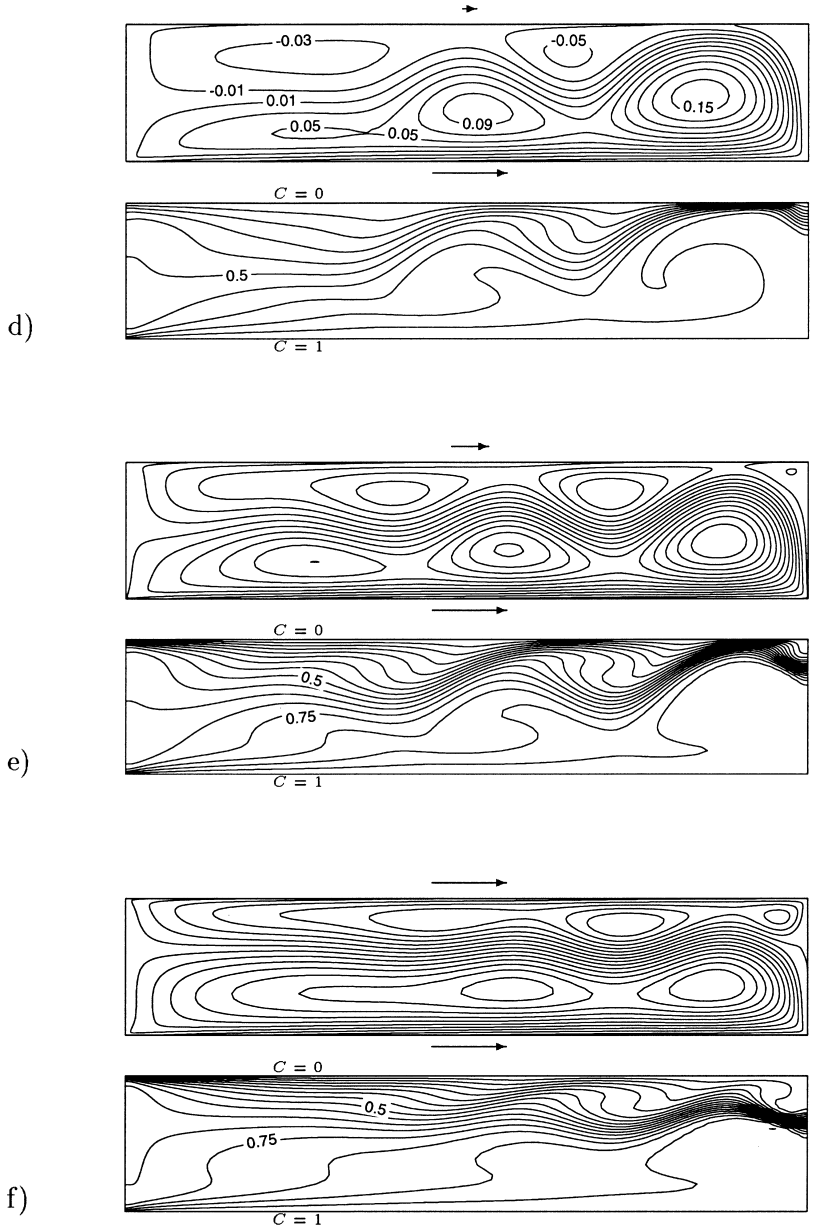

Fig. 18. *Continued.*

The location of the local maximum for heat and mass transfer depends on the concentration parameter Γ. With increasing Γ, i.e. with decreasing concentration difference between the heated and cooled walls, the location of this maximum moves in the negative direction of u, to higher velocities of the cooled wall (see Fig. 17): for $\Gamma \to \infty$ (i.e. $\Delta\omega \to 0$) it reaches $u_m \approx -2.15$.

The reason for this behavior comes from the influence of the evaporation mass flux through the heated wall on the onset of flow separation at this wall when $u < -1.6$. Such an effect has already been described in the context of boundary layer control by blowing or suction [13]. With increasing evaporation mass flux the fluid layers close to this wall are increasingly decelerated by the momentum of this flux, causing the separation point to move upstream, to smaller values of x. Therefore, with

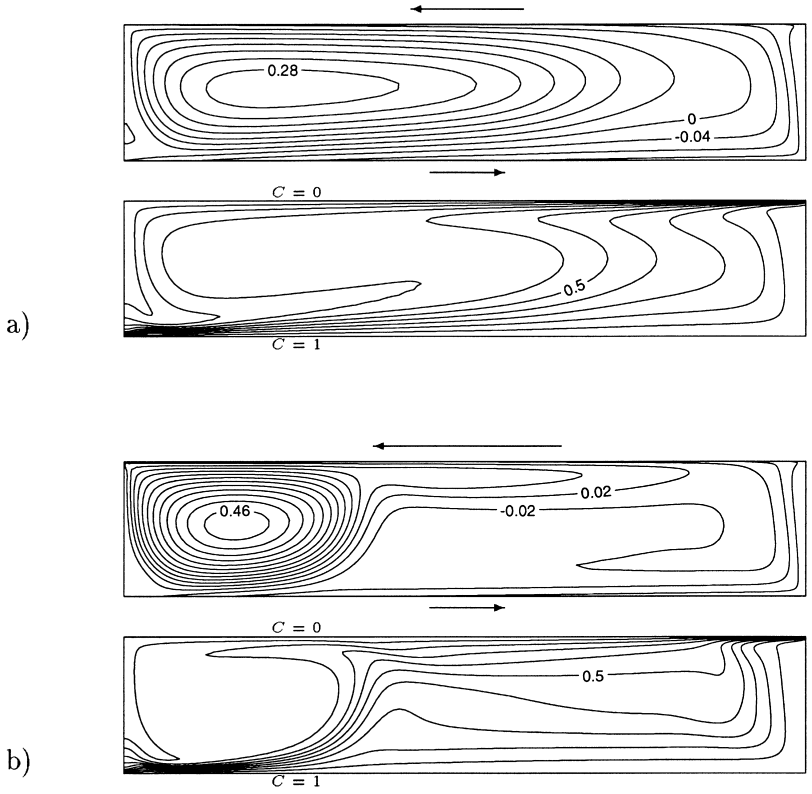

Fig. 19. Influence of the velocity ratio u on flow and concentration field for faster moving cooled wall ($l = 5$, $Re = 500$, $Pr = 0.85$, $Sc = 0.56$, $Gr = 0$, $\Gamma = 0.334$): (a) $u = -1.55$, (b) $u = -2.5$.

increasing evaporation rate, separation sets in at lower velocities of the cooled wall and shifts the location of the maximal heat and mass transfer rates towards $u = -1$.

5.3. Influence of the concentration boundary condition

Of particular importance in drying applications is the influence of the boundary condition for the species mass fraction on heat and mass transfer. Since in this paper saturation values of the solvent vapor at the heated and cooled walls are assumed, the concentration parameter is essentially a complicated function of the (absolute) wall temperatures. Therefore, it is appropriate to plot the mass flux per unit width through the interfaces (equations (32) and (33)) against the wall temperatures T_c and T_e rather than Γ. For an illustration of the effect of the concentration boundary condition, the particular system of water vapor in air at a pressure of 1 bar was chosen.

Figure 20 shows the change in the dimensionless mass flux per unit width with the condensation temperature T_c when the evaporation temperature T_e is kept constant. Results for a cavity of aspect ratio $l = 5$ are compared with

$$M_c = \log\frac{1+\Gamma}{\Gamma} \tag{54}$$

from Section 4.1 for an infinitely long cavity ($l \to \infty$) with fully developed flow.

When T_c is increased from low values, the mass transfer rate does not change significantly over a wide range of temperatures. Only when the condensation temperature comes close to the evaporation temperature T_e does the mass transfer drop drastically and vanish in the limit $T_c \to T_e$. This results essentially from the exponential relationship between the saturation concentration and the wall temperature, which also implies that changes in the evaporation temperature do have a considerably stronger influence on the mass transfer in comparison. For a water vapor/air mixture a decrease of T_e by 10 K from 368 to 358 K results, e.g., in a mass flux decrease by a factor > 2.

Figure 20 also indicates that the mass transfer rate per unit width decreases with increasing aspect ratio l of the cavity. For the relatively short cavity with $l = 5$, the mass transfer rate turns out to be about five times higher than that for the infinitely long cavity. The reason for the

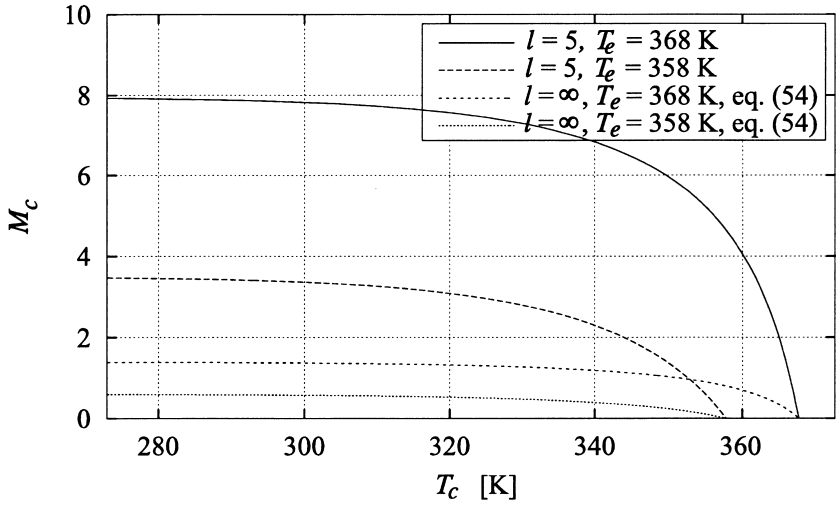

Fig. 20. Evaporation and condensation of water in the cavity: influence of the absolute wall temperatures T_e and T_c on the mass transfer, plotted in terms of the dimensionless mass flux M_c vs T_c for $Re = 500$, $u = -1$, $Gr = 0$, $Pr = 0.85$, $Sc = 0.56$ and various cavity lengths and temperatures T_e.

smaller average transfer rates for long cavities lies in an increase in the temperature and concentration boundary layer thicknesses in the direction of motion. According to equation (50), the estimated entrance length for the temperature profile is $x_d \approx 15$ of the operation parameters used in Fig. 20. In the region $x_d < x < l - x_d$ of a long cavity, the flow can be considered fully developed and heat and mass transfer are dominated by diffusion, with the asymptotic rates of an infinite cavity.

6. Conclusions

Heat and mass transfer in a lid driven cavity have been investigated in this paper with a motivation coming from process engineering, related to modeling a type of drying chamber. The results imply, when described in terms of equipment operation, information, obtained by a systematic numerical study, on ranges of stable operation with high heat and mass transfer rates, i.e. with high drying rates. It has been shown that the drying rates are enhanced by increasing web velocity and become increasingly independent of the cavity orientation because of dominance of forced convection. When the Reynolds number, as a measure of web velocity, is decreased to small values, instabilities due to buoyancy effects occur: for a vertical cavity with a downward-moving heated web they are characterized by two turning points, whereas for a horizontal cavity with a thermally unstable configuration by the occurrence of a Hopf bifurcation. When the velocity of the condensing wall is decreased with respect to that of the web, flow separation occurs on this wall and leads to a drastic reduction of the drying rate because separation reduces convection-enhancement of heat and mass transport to only a small section of the cavity. With increasing cavity length, the mean mass transfer rate per unit length decreases, due to an increase in thickness of a boundary layer that develops in the cavity. An increase of the evaporation temperature increases the mass transfer very efficiently, whereas the condensation temperature can be chosen in a wide range, relatively close to the evaporation temperature, without a significant loss in the drying rate.

Acknowledgement

The financial support of this work within the research project FOROB of the Bayerische Forschungsstiftung (Bavarian Research Foundation) is gratefully acknowledged.

References

[1] H.C. Kuhlmann, M. Wanschura, H.J. Rath, Flow in two-sided lid-driven cavities: non-uniqueness, instabilities, and cellular structures, J. Fluid Mech. 336 (1997) 267–299.
[2] G.K. Batchelor, Heat transfer by free convection across a closed cavity between vertical boundaries at different temperatures, Quart. Appl. Math. XII (1954) 209–233.
[3] R. Iwatsu, J.M. Hyun, K. Kuwahara, Mixed convection in a driven cavity with a stable vertical temperature gradient, Int. J. Heat Mass Transfer 36 (6) (1993) 1601–1608.

[4] A.A. Mohamad, R. Viskanta, Flow and heat transfer in a lid-driven cavity filled with a stably stratified fluid, Appl. Math. Modelling 19 (1995) 465–472.
[5] R.B. Mansour, R. Viskanta, Shear-opposed mixed-convection flow and heat transfer in a narrow, vertical cavity, Int. J. Heat Fluid Flow 15 (6) (1994) 462–469.
[6] O.V. Trevisan, A. Bejan, Combined heat and mass transfer by natural convection in a vertical enclosure, J. Heat Transfer 109 (1987) 105–112.
[7] R. Bennacer, D. Gobin, Cooperating thermosolutal convection in enclosures—I. Scale analysis and mass transfer, Int. J. Heat Mass Transfer 39 (13) (1996) 2671–2681.
[8] R. Bennacer, D. Gobin, Cooperating thermosolutal convection in enclosures—II. Heat transfer and flow structure, Int. J. Heat Mass Transfer 39 (13) (1996) 2683–2697.
[9] H.A. Dijkstra, E.J. Kranenborg, A bifurcation study of double diffusive flows in a laterally heated stably stratified liquid layer, Int. J. Heat Mass Transfer 39 (13) (1996) 2699–2710.
[10] J.A. Weaver, R. Viskanta, Natural convection in binary gases due to horizontal thermal and solutal gradients, J. Heat Transfer 113 (1991) 141–147.
[11] P. Ranganathan, R. Viskanta, Natural convection in a square cavity due to combined driving forces, Numerical Heat Transfer 14 (1988) 35–59.
[12] N. Alleborn, K. Nandakumar, H. Raszillier, F. Durst, Further contributions on the two dimensional flow in a sudden expansion, J. Fluid Mech. 330 (1997) 169–188.
[13] K. Gersten, H. Herwig, Strömungsmechanik, Vieweg, Braunschweig, 1992.
[14] P.J. Roache, Computational Fluid Dynamics, Hermosa, Albuquerque, 1972.
[15] R.B. Bird, W.E. Stewart, E.N. Lightfoot, Transport Phenomena, John Wiley and Sons, New York, 1960.
[16] N. Alleborn, H. Raszillier, F. Durst, Direct condensation drying—a concept for film dryers, Proceedings of the Second European Coating Symposium (ECS '97), University Louis Pasteur, Strasbourg, 1997 (in press).
[17] E.L. Allgower, K. Georg, Numerical Continuation Methods, Springer-Verlag, Berlin, 1990.
[18] R.B. Lehoucq, D.C. Sorensen, P. Vu, ARPACK: an implementation of the Implicitly Re-started Arnoldi Iteration that computes some of the eigenvalues and eigenvectors of a large sparse matrix, Available from netlib@ornl.gov under the directory scalapack.